J. Fluid Mech. (1992), *vol.* 240, *pp.* 167–195
Printed in Great Britain

On transition due to three-dimensional disturbances in plane Poiseuille flow

By BARBRO G. B. KLINGMANN
Department of Gasdynamics, Royal Institute of Technology, S-100 44 Stockholm, Sweden

(Received 12 September 1991)

The purpose of the present study is to characterize the process of laminar–turbulent transition at Reynolds numbers which are subcritical from the two-dimensional linear point of view. The development of a point-like disturbance was studied in an air flow channel with hot-wire anemometry at a Reynolds number of 1600. Localized disturbances were triggered at one of the walls and their development followed downstream by traversing the hot-wire probe in the streamwise direction over a distance of 90 half channel heights, as well as in the normal and spanwise directions. The disturbance evolved into elongated streaky structures with strong spanwise shear (i.e. normal vorticity) which grew in amplitude and streamwise extension and thereafter either decayed or gave rise to a turbulent spot. The results indicate that the mechanism underlying the initial growth is a linear one resulting from the coupling between the normal velocity and the normal vorticity, as described by the three-dimensional linear equations. The nonlinear development of the structure leads to the formation of intense normal shear layers and the appearance of oscillations and 'spikes', which multiply and form the rear or a turbulent spot.

1. Introduction

Natural transition is often thought of as the result of a localized, transient disturbance which may trigger the growth of unstable waves. Classical Orr–Sommerfeld theory deals with the stability of linear Tollmien–Schlichting (TS) waves with a definite frequency or wavenumber at a given Reynolds number. In the flat-plate boundary layer, the propagation velocity of neutrally stable TS waves is typically about 40% of the free-stream velocity (U_∞). According to the so-called Squire theorem, a three-dimensional (3D) TS wave can be transformed into a corresponding two-dimensional (2D) wave which becomes unstable further upstream, implying that, at a given downstream position, the 2D wave will have gained a larger amplitude than the 3D wave and is therefore most likely to be observed experimentally. Two-dimensional waves with a definite frequency can be artificially generated by a vibrating ribbon which induces a TS wave in the boundary layer. However, the experiments by Klebanoff, Tidstrom & Sargent (1962) showed that there is a strong tendency for the flow to develop a 3D structure before transition to turbulence occurs. Nonlinear interactions between 2D and 3D waves then lead to the formation of Λ-shaped vortex structures. Depending on the amplitude of the 2D wave, these may either appear in an aligned or in a staggered configuration. The aligned configuration is the result of the interaction of a finite amplitude TS wave with 3D wave components with the same (fundamental) frequency. This was the case observed by Klebanoff *et al.* Transition is preceded by the formation of 3D travelling high-shear layers, which are associated with a strong inflexion in the local velocity

profile, and with the appearance of 'spikes' at the downstream 'head' of the vortex structure. At lower amplitudes of the fundamental TS wave, interactions with 3D waves at half of the frequency are favoured. The powerful nonlinear resonance which results from the subharmonic interaction was first described by Craik (1971), and Kachanov & Levchenko (1984) experimentally confirmed that this mechanism is active in the transition in the flat plate boundary layer. In this case, transition takes place by a gradual filling of the spectrum without high-shear layers or spikes ever appearing.

If the initial disturbance itself is 3D and localized in space, yet another effect comes into play, namely the algebraic growth mechanism. While seeking to explain the bursting process in turbulent flow, Landahl (1975) found that a localized disturbance in the normal velocity (v) induces a non-decaying disturbance in the velocity parallel to the wall, provided the streamwise integral of v is non-vanishing (in wavenumber space, this means that v has contributions at zero streamwise wavenumber, $\alpha = 0$). This 'permanent scar' is convected downstream at the local mean flow velocity, $U(y)$, i.e. the propagation speed of the resulting flow structure varies with the normal position (y) through the shear layer. Since perturbations located near the wall propagate at a lower speed than those parts which are located away from the wall, the perturbation structure is continuously elongated during its downstream travel. The inviscid analysis of Landahl (1980) shows that the flow structure elongates at a rate proportional to time. Combined with a bounded growth in the wall-parallel velocity, this gives an energy growth rate at least as fast as time, i.e. the energy growth is algebraic. This result is valid for any inviscid shear flow subject to an initially 3D disturbance in v with contributions at $\alpha = 0$, and the phenomenon is essentially linear and inviscid. It will henceforth be referred to as the linear 3D growth mechanism.

Henningson (1988) analytically obtained a solution to the linear inviscid initial-value problem for the case of a piecewise linear velocity profile approximating the plane Poiseuille flow. The initial disturbance consisted of a pair of counter-rotating vortices. His analysis shows that the energy growth is due to a linear coupling between the normal velocity and the velocity component parallel to the wall and perpendicular to the wave vector. This velocity component is proportional to the normal vorticity (η). He also showed that the inviscid solution consists of both a dispersive part and a part which is a function of $x - U(y)t$. This demonstrates another characteristic feature of the linear 3D growth mechanism, namely the absence of spanwise spreading. The spanwise propagation of the resulting flow structure is only due to the dispersion of oblique modes related to the critical layer, and may be expected to be weak when these modes are damped.

Owing to viscosity, the time of energy growth is limited, so that flow structures which have not, during their growth phase, evolved in such a way as to cause transition will ultimately decay. The linear 3D viscous initial-value problem was first treated by Gustavsson (1991), and was further elaborated by Henningson & Schmid (1991). The linear coupling between v and η is in this case provided by the eigenmodes of the Orr–Sommerfeld equation, which appear as driving terms in the 3D Squire equation. This means that a single Orr–Sommerfeld (v-) mode excites the whole spectrum of Squire (η-) modes with different propagation velocities and different y-distributions. This driving may lead to a considerable energy growth associated with the normal vorticity even though v is decaying. The mechanism is therefore possible at Reynolds numbers below those at which TS waves become unstable – in fact, the analysis of Gustavsson shows that there is no low-Reynolds-number limit for the

linear 3D growth mechanism to be active. Gustavsson also discussed the nonlinear effects which may arise as the perturbation grows beyond the linear stage. He showed that the nonlinear terms are associated with streamwise gradients, but vanish for $\alpha = 0$.

With the object of modelling the natural development of turbulent spots, Gaster & Grant (1975) used a localized transient initial disturbance to excite a wave packet in the flat-plate boundary layer. The initial disturbance was introduced into the boundary layer in the form of an air jet issuing from a small hole at the wall. Hot-wire measurements made at the boundary-layer edge revealed a wave packet with propagation speeds and growth characteristics in excellent agreement with the predictions of Gaster (1975) based on the superposition of TS waves.

On the other hand, in many other experiments in the flat-plate boundary layer, it has been observed that a 3D initial disturbance can give rise to a flow structure which is not consistent with a TS wave packet. Such observations were reported by Vasudeva (1967), Wygnanski (1981), Amini & Lespinard (1982), Chambers & Thomas (1983), Grek, Kozlov & Ramazanov (1985) and Lismonde (1987). Most of these authors report that the observed flow structure had a propagation velocity of 0.5–0.6 U_∞ at the rear and 0.9 U_∞ at the front, in contrast to the propagation velocity of the linear TS wave packet (about 0.4 U_∞) studied by Gaster & Grant (1975). In most cases (the experiment of Vasudeva being an exception) the observed structure was quite narrow in the spanwise direction and had a complicated 3D structure. Amini & Lespinard (1982) found that the initial disturbance must penetrate the boundary layer in order to give rise to a turbulent spot, and therefore they used an initial jet of large intensity. This gave rise to a propagating flow structure characterized by longitudinal streaks of alternating high and low velocity, which they termed an 'incipient spot'. Low-velocity streaks were found to join at the front of the structure giving it a U-shaped form. At the stage of transition, isolated spike-like regions of low-velocity, associated with a strong local inflexion in the velocity profile, appeared at the back of the U-shaped structure. The spikes were seen to multiply at the rear, giving rise to a turbulent spot. Detailed hot-wire measurements of this flow structure were later carried out by Lismonde (1987) in the same set-up. His results show that transition is preceded by an oscillating spanwise motion at the front, associated with a corresponding fluctuation in the wall pressure, which results in a loss of the spanwise symmetry of the structure.

More recently, Tso, Chang & Blackwelder (1990) showed that an initial disturbance in the form of a jet gives rise to (at least) two different types of wave packet, and that the amplitude of the initial jet determines which one will dominate over the other. For low amplitudes, they found the dominant one to be a slowly growing wave packet which propagated downstream at the typical speed of the TS waves, as in the case of Gaster & Grant (1975). For larger initial amplitudes, however, a strongly growing transient causes transition. The transient disturbance had a propagation velocity of 0.5 U_∞ at the rear and 0.9 U_∞ at the front, in agreement with the findings of Amini & Lespinard (1982), and gave rise to a turbulent spot with the same leading- and trailing-edge celerities.

The simultaneous occurrence of these two different transition scenarios has been further elucidated in a series by Cohen, Breuer & Haritonidis (1991), Breuer & Haritonidis (1990) and Breuer & Landahl (1990), in which the evolution of a point-like disturbance is studied both numerically and experimentally. As found by Tso *et al.* (1990), the disturbance evolves in completely different ways depending on the initial condition. In the case studied by Cohen *et al.*, a weak disturbance develops into

a bow-shaped wave packet in the outer part of the boundary layer, as observed by Gaster & Grant (1975). Transition occurs by a gradual filling of the spectrum owing to nonlinear subharmonic interactions. This development was theoretically predicted by Zelman & Smorodsky (1990). During this stage, 3D wave components are strongly growing due to the Craik resonance mechanism, and the lift-up effect described by Landahl (1975, 1980) gives an important contribution to the energy associated with the wall-parallel velocity components. For a larger and more concentrated initial disturbance (see Breuer & Haritonidis) a TS wave packet evolves in the outer part of the boundary layer, and in addition to this, an inclined shear layer structure caused by the lift-up effect develops in the interior of the boundary layer. The shear layer has a lower propagation velocity near the wall than in the outer parts of the boundary layer, which results in a tilting and stretching of the shear layer. The experimental results were compared to those obtained by solving the linear inviscid initial-value problem. This simplified model was able to qualitatively reproduce the main features of the early development of the shear layer observed in the experiment, demonstrating that the mechanism of initial transient of 3D shear layers is basically linear and inviscid. The shear structure decays further downstream, and leaves only the growing wave packet. For stronger disturbances, the numerical simulations of Breuer & Landahl show that the inclined-shear-layer structure dominates over the wave part of the disturbance. The nonlinear intensification of the shear layers makes them susceptible to wavelike secondary instabilities, which may lead to turbulent breakdown.

Transition in plane Poiseuille flow can occur at Reynolds numbers substantially below the critical Reynolds number for Tollmien–Schlichting wave growth. This means that transition mechanisms involving the growth of TS waves are not at work. These so-called 'by-pass' mechanisms have generally been thought of as nonlinear. However, the linear 3D initial growth provides a powerful mechanism for the growth of local disturbances which may be present in the form of background noise or random disturbances convected downstream from the channel inlet.

Henningson (1991) solved the viscous initial-value problem for a localized disturbance in plane Poiseuille flow by decomposing the initial disturbance into Orr–Sommerfeld and Squire modes and calculating the linear time evolutions of the induced vorticity modes. The linear model was able to reproduce essential features of the initial evolution obtained by full Navier–Stokes simulations. Using Navier–Stokes simulations, Henningson, Lundbladh & Johansson (1991) studied the evolution of a localized disturbance in plane Poiseuille flow from its linear initial stages to the birth of a turbulent spot. They were able to separate the linear and nonlinear parts of the evolving flow structure by varying the amplitude of the initial disturbance. Beyond the linear stage, nonlinear interactions between (α, β)-components generate contributions at $(0, 2\beta)$, which in turn generate contributions at $(0, 3\beta)$, while higher α-components are rapidly damped (β denotes the spanwise wavenumber). As a result of this process, which Henningson *et al.* termed the 'β-cascade', the $\alpha = 0$ components (which are crucial in the linear initial development) are continually regenerated at the nonlinear stage, resulting in an enhancement of the normal and spanwise shear layers and of the streamwise elongation of the flow structure. Another consequence of this nonlinear development is that the perturbation structure becomes independent of the initial disturbance.

This paper presents experimental results which show that the 3D linear growth mechanism can be an important factor in the transition process in plane Poiseuille flow. It is believed that these results may also be relevant for other wall-bounded

shear flows where 3D disturbances are present, and particularly in cases where mechanisms based on 2D TS wave growth are not operative, e.g. transition due to leading-edge disturbances or free-stream turbulence in boundary layers, or transition in plane Couette or pipe flow. Section 2 describes the experimental apparatus. In §3, observations on the evolution of a point-like disturbance are examined in order to determine to what extent the initial development is governed by the linear 3D mechanism. The results are obtained using an initial disturbance amplitude which is half as large as the amplitude required to generate a turbulent spot. Some features of the 3D linear eigenmodes for parameters present in the experiments are presented and compared to the experiments. Sections 4 and 5 show the evolution of a disturbance initiated with an amplitude which is large enough to trigger spot formation. It evolves in a similar way to the subcritical disturbances up to the point of maximum growth, at which wavelike instabilities are observed. The breakdown to turbulence is associated with intense inclined shear layers and the appearance of 'spikes'. The relation of these observations to similar observations in other transition studies is discussed in the concluding remarks.

2. Experimental set-up

2.1. *Flow apparatus*

The general outline of the experimental set-up is shown in figure 1. The flow apparatus was a plane channel consisting of two 2 m long and 10 mm thick parallel glass plates separated by distance bars on the sides. The channel height ($2h$) was 8.2 mm with a spanwise variation less than ± 0.1 mm, and its width was 0.83 m, giving an aspect ratio of 101. Air was fed into the channel from a fan with variable flow rate and distributed through a perforated pipe followed by two turbulence damping screens and a contraction of 40 : 1 before it entered the test section through a carefully polished entrance. The centreline velocity (U_{CL}) was adjusted to about 6 m/s, giving a Reynolds number ($Re = U_{CL}h/\nu$) of about 1600 at a fluid temperature of 22 °C. The background disturbance level of the flow was less than 0.15% of U_{CL} at this Re. U_{CL} was determined to within ± 0.1 m/s at the actual measurement station using a traversable total head probe in combination with static pressure taps located along the upper channel wall. At $Re = 1600$, the parabolic velocity profile could be expected to be fully developed after about $170h$. Disturbances were introduced into the flow in the form of an air jet emanating from a 1 mm diameter hole in the upper channel wall ($y/h = 1$) $200h$ downstream of the channel inlet. The jet was produced by a loudspeaker, which was fed with a single square wave pulse of short duration (2 ms). The jet velocity (V_j) caused by the loudspeaker was proportional to the input voltage.

Klingmann & Alfredsson (1990) used the same apparatus to study the formation of turbulent spots at $Re = 1600$, and found a narrow range of V_j/U_{CL} between 1.5 and 1.6, within which the probability of spot formation increased from 0 to 1. In the present study, disturbances resulting from three different initial jet amplitudes were studied, namely $V_j/U_{CL} = 0.75$, 1.4 and 1.6, which will be referred to as subcritical, near critical and critical respectively.

2.2. *Traversing mechanism*

The streamwise velocity component was measured with a single hot-wire using a CTA anemometer DISA 55M01. The hot wire had a sensor length of 0.8 mm and a wire diameter of 2.5 μm, and could be traversed manually in the streamwise (x),

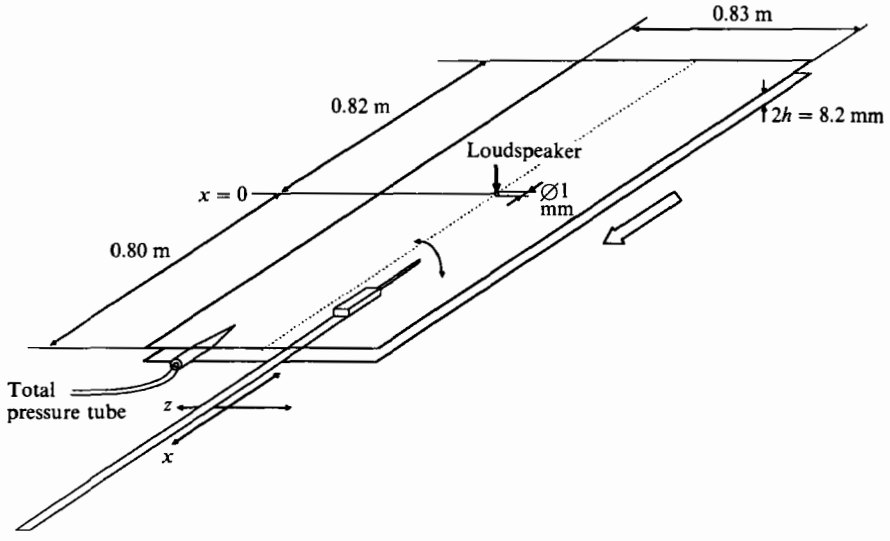

FIGURE 1. Experimental apparatus.

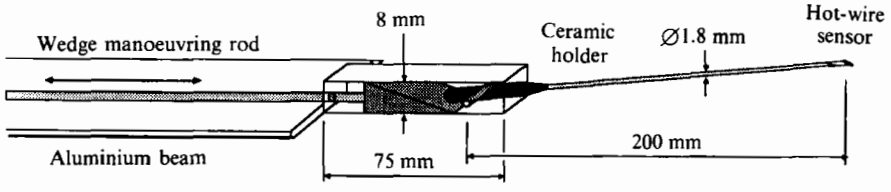

FIGURE 2. Traversing mechanism.

normal (y) and spanwise (z) directions. The hot-wire prongs were supported by a 185 mm long circular ceramic beam, with a diameter of 1.8 mm. It was traversed in the normal direction by rotating the probe around the z-axis by means of a moveable wedge manoeuvred with a micrometer, as shown in figure 2. About 65% of the channel height was covered. The normal position of the hot wire was an approximately linear function of the wedge position, and the accuracy in the normal position was ± 0.015 mm (0.35% of h). The probe and the rotation mechanism were mounted on a 300 mm long and 4 mm thick aluminium bar which could be traversed in the x- and z-directions by means of two perpendicular guide systems, which were manually adjustable to within 0.2 mm.

2.3. *Measurement technique and data evaluation*

The hot-wire was calibrated against the Poiseuille profile in the undisturbed channel flow, i.e. the normal position was translated into the corresponding velocity in a parabolic velocity profile. A calibration function recommended by Johansson & Alfredsson (1982),

$$U = k_1(E^2 - E_0^2)^{1/n} + k_2(E - E_0)^{\frac{1}{2}},$$

(where E is the anemometer output voltage at the velocity U, and E_0 is the voltage at zero velocity) was found to fit the general shape of the calibration curve well, over large velocity intervals, giving an error below 0.6% of U_{CL} for all calibration points. An overheat ratio of 35% was used. The major sources of inaccuracy in the velocity

measurements were due to (i) the sensitivity of the hot wire to minor temperature variations during the course of a measurement session, and (ii) the inaccuracy in the determination of the normal position. The first of these two problems was eliminated by recalibrating the hot wire as soon as a temperature drift was observed.

The triggering and data sampling were controlled by a PDP11, using a sampling rate of 2 kHz. Between 10 and 50 data sets covering the passage of the disturbance structure were collected at each measurement position, transformed into velocity using the previously established calibration curve, and thereafter ensemble averaged on the PDP11. Since most of the results concern laminar (deterministic) flow behaviour, the ensemble averaging was mainly performed in order to eliminate signal noise. In the final data evaluation, which was carried out on a Macintosh SE/30, the disturbance velocity was evaluated by subtracting the undisturbed velocity from the ensemble at each measurement position. Since the disturbance velocity varied less with normal position than the Poiseuille flow profile, its accuracy is almost unaffected by minor deviations from the exact normal position. The final accuracy in the disturbance velocity is estimated to be within 0.5%.

All quantities below are made non-dimensional using h and U_{CL}. Unless otherwise stated, the presented results are deterministic, so that the ensemble average is representative of a single realization.

3. Subcritical disturbances

Subcritical disturbances were triggered using an initial disturbance about half as large as that required to give rise to a turbulent spot. Measurements were made by traversing a single-wire probe in the y- and z-directions at fixed downstream positions. The distance between y-positions was 0.15 in the centre of the channel and 0.035 closer to the walls, whereas the distance between z-positions was constant and equal to 0.25.

3.1. *Initial spread*

Figure 3 shows a cross-channel view of contours of streamwise velocity perturbation (u) at the spanwise centreline ($z = 0$) close to the injection point, as a function of time. Note that the time axis is reversed, so that the flow direction is from left to right. At $x = 2$, a concentrated core of low-speed fluid is seen at $y = 0.35$. This is the direct consequence of the displacement of low-velocity fluid from the upper wall ($y = 1$) towards the centre of the channel by the initial jet, and it induces an increase in the velocity at the opposite side of the channel. At $x = 5$, the low-speed core has penetrated to the channel centreline ($y = 0$). It is decreasing in amplitude (from -0.475 to -0.375), whereas the induced perturbations in the lower part of the channel have increased (from 0.025 to 0.075). At $x = 15$, the initial disturbance continues to fade, while the induced perturbations increase. The near wall parts of the structure propagate more slowly than in the part located at the centre of the channel, resulting in a more and more elongated normal shear structure. At $x = 30$, a low-velocity lump moving ahead of the structure remains as a reminiscence of the initial jet. Also the induced perturbations seem to be decreasing in amplitude. However, the structure as a whole is still in a process of growth, expanding and intensifying in the spanwise and streamwise directions. Strong normal and spanwise shear layers are found away from $z = 0$. As a consequence of the asymmetric way in which the initial disturbance was introduced, the induced perturbation structure extends further upstream and the shear is stronger in the lower part of the channel than in the upper part.

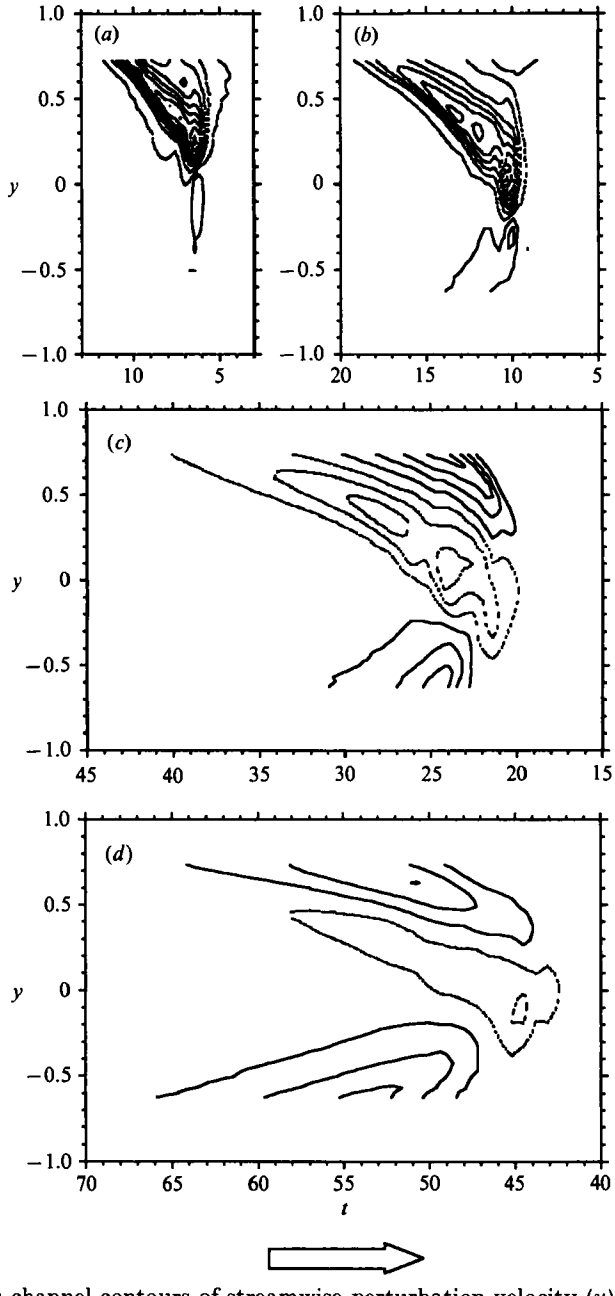

FIGURE 3. Cross-channel contours of streamwise perturbation velocity (u) at $z = 0$ for subcritical initial disturbance amplitude ($V_1 = 0.75$). Contour spacing is 0.5% of U_{CL}. (a) $x = 2$; min -0.475; max 0.025. (b) $x = 5$; min -0.325; max 0.075. (c) $x = 15$; min -0.125; max 0.175. (d) $x = 30$; min -0.075; max 0.125.

3.2. *Evolution and spanwise structure*

The streamwise extension of the disturbance was found to increase almost uniformly with downstream distance. Making use of this property, the conical coordinate,

$$\xi = x/(t-t_0),$$

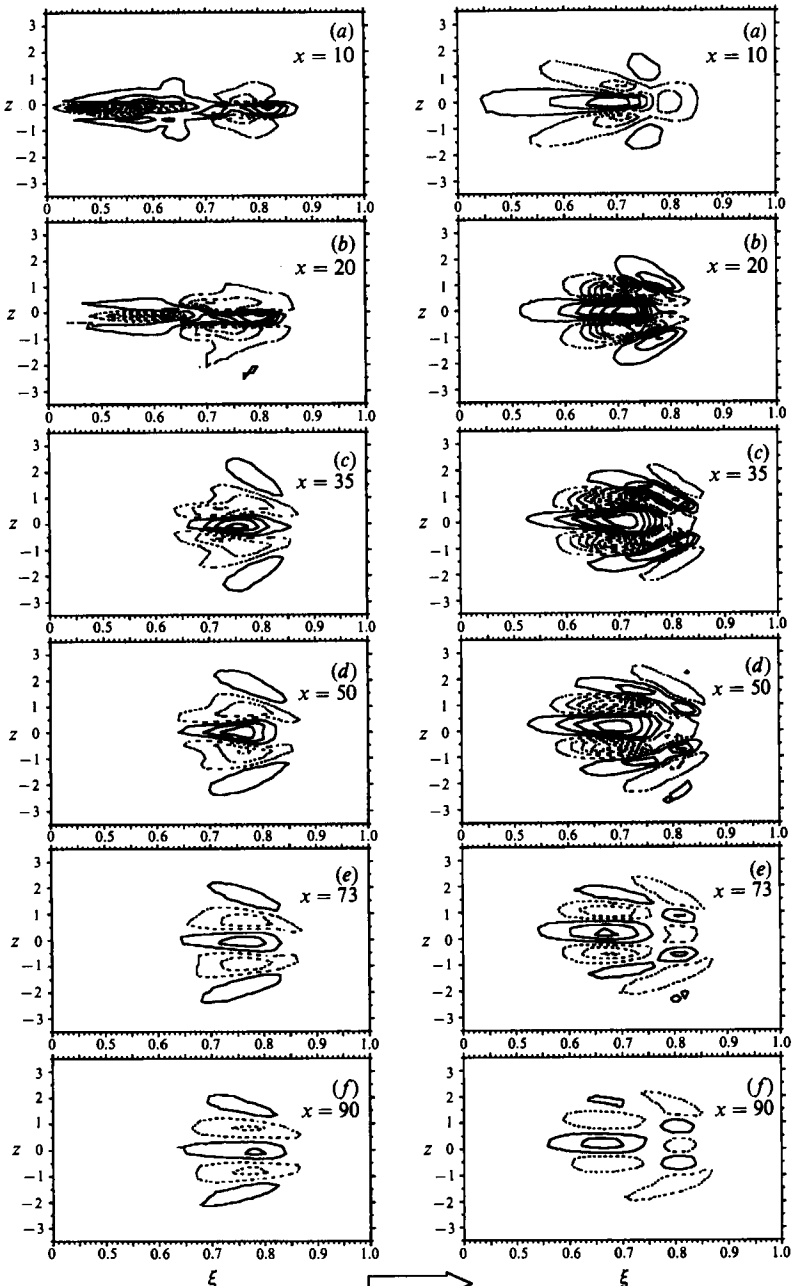

FIGURE 4 FIGURE 5

FIGURE 4. Spanwise contours of u at $y = +0.5$ for $V_1 = 0.75$. Levels are $\pm 1\%$, $\pm 3\%$, etc.

FIGURE 5. As in figure 4 for $y = -0.5$.

is introduced, which can be directly interpreted as the propagation velocities for the different parts of the structure. Figures 4 and 5 show the spanwise distribution perturbation velocity (u) in the (ξ, z)-plane $y = \pm 0.5$ respectively, obtained by spanwise traverses at a number of fixed x-positions ($x = 10$, 20, 35, 50, 73 and 90). The level spacing is 2% of U_{CL}. A good representation of the near-uniformity of the

downstream growth was obtained choosing a value of $t_0 = 3.6$, corresponding to an initial time delay of 2.5 ms, which is of the order of the effective triggering time.

At $x = 10$, the strong negative disturbance velocity resulting from the initial jet can be seen at the upstream (left-hand) side of the disturbance in the upper half of the channel (figure 4*a*). It induces a pattern of alternating high- and low-velocity regions which are also seen in the opposite part of the channel. While the effect of the initial jet itself decays further downstream, the induced pattern develops oblique lobes at the front. These are swept back as they travel downstream, evolving into elongated streaks of alternating high and low velocity. The spanwise position of the streaks is fairly constant at all downstream positions, and the small spreading is mainly due to the appearance of new streaks. Hence there is no spanwise propagation. Owing to this regular spanwise structure, the amplitude of the streamwise perturbation velocity (u) can be taken as approximately proportional to its spanwise gradient ($\partial u/\partial z$). The measurements of Breuer & Haritonidis (1990) for a similar case in the boundary-layer flow show that the spanwise velocity (w) is about half as large as the streamwise velocity, and that its streamwise gradients are much smaller than $\partial u/\partial z$. The normal vorticity ($\eta = \partial u/\partial z - \partial w/\partial x$) may therefore be approximated by $\partial u/\partial z$.

The streaks extend further upstream in the lower part of the channel, i.e. on the side opposite to the triggering, and the perturbation amplitude is higher there. The inner streaks in figure 5 are seen to join at the front, giving a V-shaped low-velocity region pointing in the downstream direction. The front of the structure propagates at a velocity of $\xi = 0.82$, whereas the rear is found at $\xi = 0.65$ in the upper half of the channel and at $\xi = 0.55$ in the lower part. The spanwise gradients are most intense for ξ between 0.65 to 0.75, and the perturbation velocity is largest at the central low-speed streaks ($z = \pm 0.85$), with u reaching a maximum amplitude of 13% at $x = 35$. Past $x = 50$, the local intensity of u decay in both the upper and the lower parts of the channel, while the streamwise extension of the structure is still growing. Note that a constant length in the conical coordinate system means a constant streamwise elongation in physical space (see also Klingmann 1991). This is a characteristic feature of the inviscid linear 3D growth mechanism of Landahl (1980). Another characteristic present here is the lack of spanwise propagation (cf. Breuer & Landahl 1990). These observations indicate that the evolution of the perturbation structure is governed by the linear 3D mechanism, although nonlinear effects should be expected at the present u-amplitudes.

3.3. *Cross-channel distribution*

Isocontours of the streamwise velocity ($U = U_{\text{pois}} + u$) are shown in figure 6 for two different spanwise positions. $z = 0.85$ corresponds to the position of the most intense low-velocity streak, and $z = -1.35$ to the outer part where the streak pattern is oblique. Inclined layers of enhanced normal shear are seen near $\xi = 0.8$ and near $\xi = 0.65$, corresponding to the central low-velocity region in figure 5(*c*). The loci where U is equal to the propagation velocity ξ are marked with a coarse line. To the left of this line, the local velocity is higher than the propagation velocity. This line tends to be aligned with the shear layers, showing that they propagate downstream at the velocity of the local flow. This behaviour is again characteristic of the linear 3D mechanism, by which horizontal velocity disturbances are carried downstream with the local velocity of the basic flow. However, the shear layer in figure 6 does not follow the undisturbed flow velocity (U_{pois}) but instead moves at the disturbed velocity U, indicating a nonlinear modification of the flow.

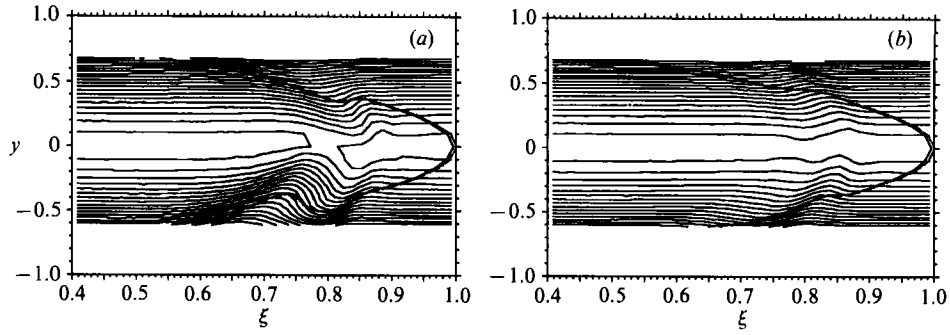

FIGURE 6. Cross-channel contours of the streamwise velocity $U = U_{\text{pois}} + u$ at $x = 35$. Levels are 0.025, 0.075, etc. $V_i = 0.75$. (*a*) $z = 0.85$. (*b*) $z = 1.34$.

Figure 7 shows cross-channel views of the perturbation velocity at $x = 35$ for different times through the passage of the disturbance structure. A system of alternating high- and low-velocity streaks is seen to split off the centre ($y = z = 0$) at the front and extend towards the upper and lower channel walls respectively. The front of the structure appears first as a low-velocity perturbation at $y = z = 0$, $\xi = 0.90$, which at $\xi = 0.85$ is divided into a pair of low-speed streaks tending towards the upper part of the channel and centred at $z = \pm 0.5$, whereas a pair of high-speed streaks appears in the lower part. At $\xi = 0.82$, a new pair of low-speed streaks splits away from the centre above the high-speed region. They move outward to a spanwise position of $z = \pm 0.85$, and further downstream approach the lower wall. The perturbation velocity is most intense at $\xi = 0.74$, reaching an amplitude of almost 15%. At that time they are centred at $y = -0.4$. Both normal ($\eta \approx \partial u/\partial z$) and spanwise ($\approx \partial u/\partial y$) perturbation vorticity is present. The inclination of the shear layers in the (y, z)-plane may also be an indication of streamwise vorticity ($= \partial v/\partial z - \partial w/\partial y$) transporting low-speed fluid from the wall towards the interior of the channel and displacing it outwards in the spanwise direction. These observations give a picture of two oblique V-shaped shear layers, with downstream pointing 'heads' which join at the centre of the channel, and 'legs' which extend upstream towards the upper and lower walls respectively. The structure is reminiscent of the $\wedge$-vortices which characterize the TS wave transition. However, it will be seen in the following sections that the V-shaped structure does not play the same role as a $\wedge$-vortex in the transition to turbulence.

3.4. *Energy growth and decay*

The data in figures 4 and 5 were transformed into frequency and spanwise wavenumber space using a double Fourier transform defined by

$$\hat{u}(\omega, \beta) = \int_0^T \int_{-\frac{1}{2}Z}^{\frac{1}{2}Z} u(t, z) \exp\{-\mathrm{i}\omega t - \mathrm{i}\beta z\} \, \mathrm{d}z \, \mathrm{d}t,$$

(where T is the maximum time period and Z the spanwise domain), and approximated by

$$\hat{u}(\omega_m, \beta_n) = \sum_{j=0}^{M} \sum_{k=-\frac{1}{2}N}^{\frac{1}{2}N} u(t_j, z_k) \exp\{-\mathrm{i}\omega_m t_j - \mathrm{i}\beta_n z_k\} \, \Delta z \, \Delta t,$$

with

$$t_j = j\Delta t, \quad \omega_m = 2\pi m / M\Delta t,$$

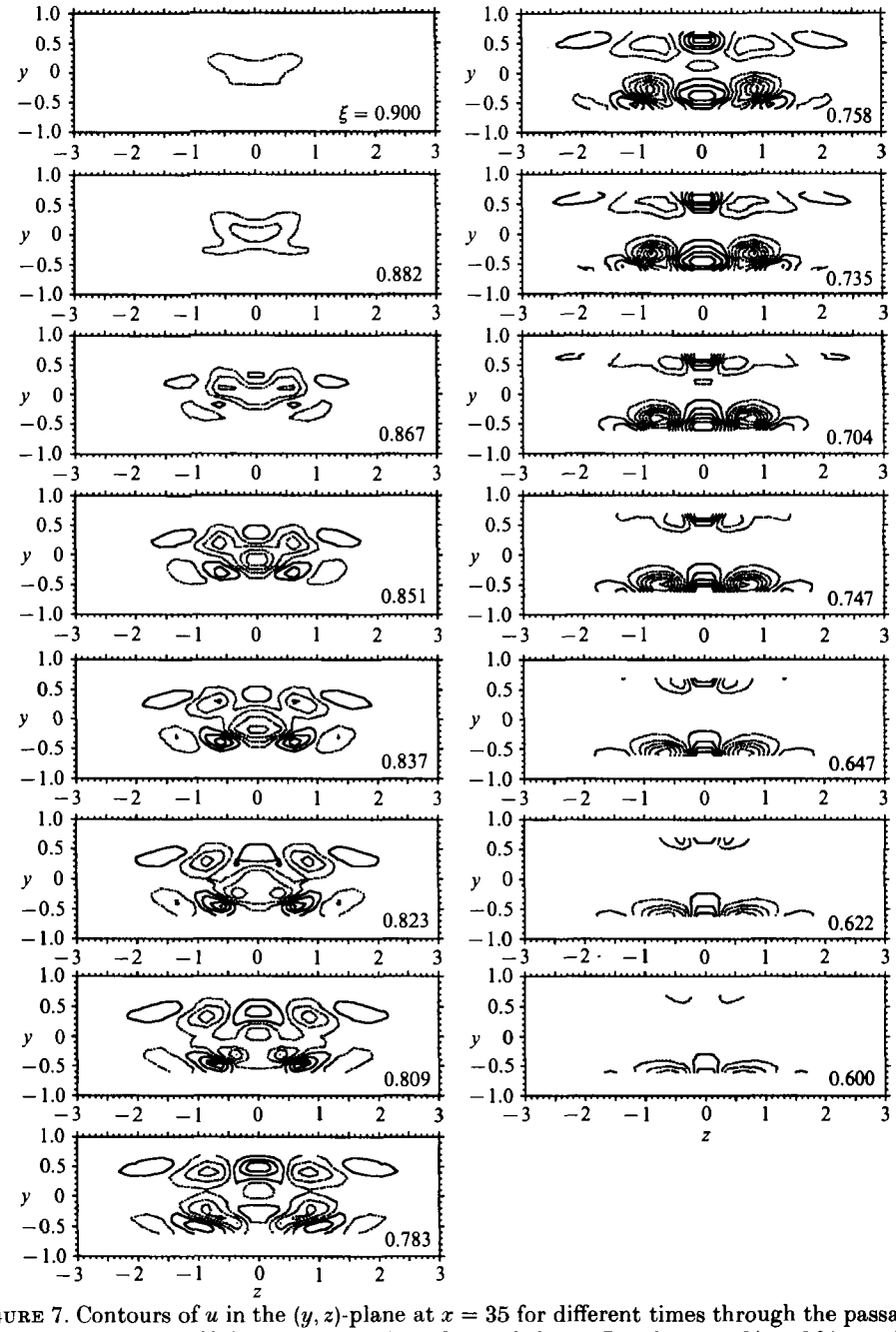

FIGURE 7. Contours of u in the (y, z)-plane at $x = 35$ for different times through the passage of the disturbance structure. Values of ξ are indicated in each figure. Levels at $\pm 1\,\%$, $\pm 3\,\%$, etc. $V_1 = 0.75$.

and $$z_k = k\Delta z, \quad \beta_n = 2\pi n/N\Delta z,$$

Δt is the time between two successive samples (0.72 in non-dimensional units) and Δz the distance between the spanwise measurement positions (0.244). The number of timesteps (M) was 512, covering the evolution of the disturbance at all streamwise positions measured. The number of spanwise measurement points was increased with the undisturbed (zero) value up to $N = 64$.

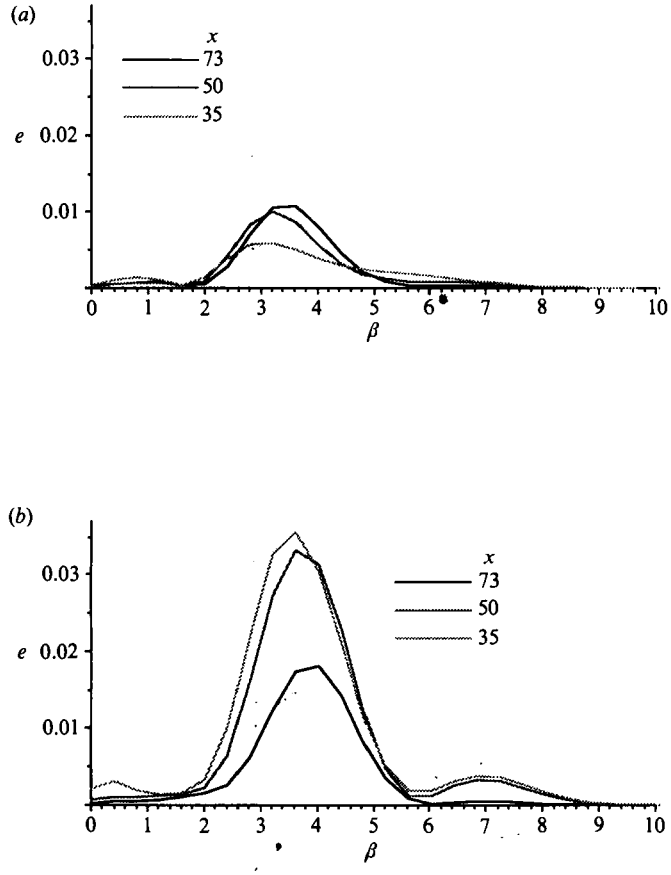

FIGURE 8. Spanwise energy distribution $e_2(\beta)$ obtained from data shown in figures 3 and 4. (*a*) $y = 0.5$. (*b*) $y = -0.5$.

From the Parseval identity, the perturbation energy per unit length normal to the wall in the (t, z)-plane is

$$E = \frac{1}{2}\int_0^T \int_{-\frac{1}{2}Z}^{\frac{1}{2}Z} u^2(t,z)\,\mathrm{d}t\,\mathrm{d}z = \tfrac{1}{8}\pi^2 \int_{-\infty}^{\infty}\int_{-\infty}^{\infty} |\hat{u}(\omega,\beta)|^2\,\mathrm{d}\omega\,\mathrm{d}\beta.$$

The quantities

$$e_1(\omega) = \tfrac{1}{4}\pi \int_{-\infty}^{\infty} |\hat{u}(\omega,\beta)|^2\,\mathrm{d}\beta \approx \frac{1}{2}\sum_{n=-\frac{1}{2}N}^{\frac{1}{2}N} |\hat{u}(\omega,\beta_n)|^2/N\Delta z,$$

$$e_2(\beta) = \tfrac{1}{4}\pi \int_{-\infty}^{\infty} |\hat{u}(\omega,\beta)|^2\,\mathrm{d}\omega \approx \frac{1}{2}\sum_{m=-\frac{1}{2}M}^{\frac{1}{2}N} |\hat{u}(\omega_m,\beta)|^2/M\Delta t,$$

are functions of angular frequency and spanwise wavenumber respectively, which are independent of M, N, Δt and Δz, and will be referred to as the energy densities, since E can be expressed in terms of e_1 and e_2 as

$$E = \int_0^T e_1(\omega)\,\mathrm{d}\omega = \int_{-\frac{1}{2}Z}^{\frac{1}{2}Z} e_2(\beta)\,\mathrm{d}\beta.$$

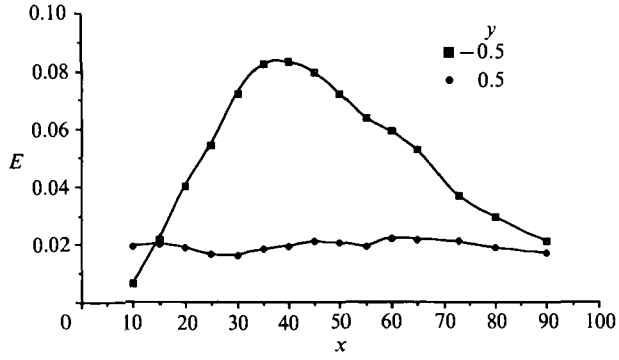

FIGURE 9. Evolution of energy per unit normal length in the planes $y = \pm 0.5$. $V_i = 0.75$.

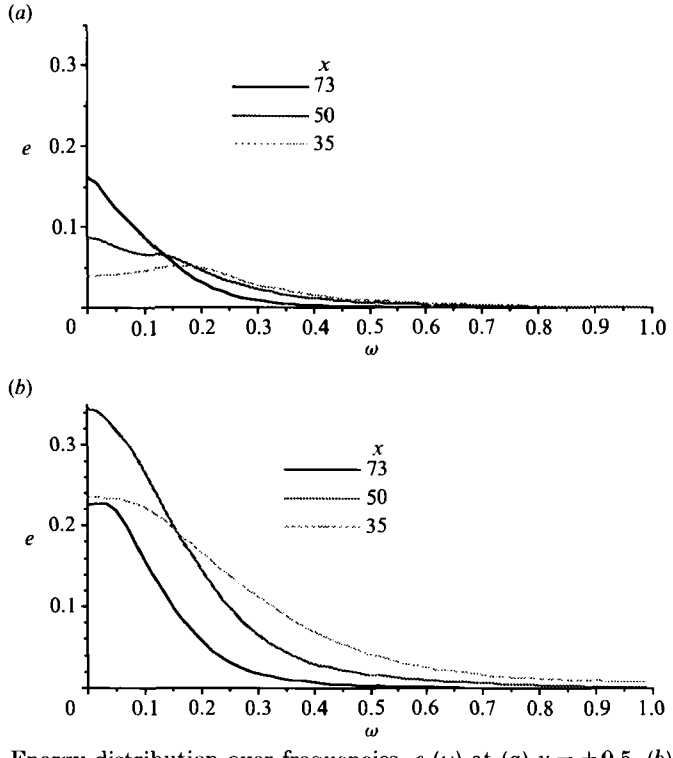

FIGURE 10. Energy distribution over frequencies, $e_1(\omega)$ at (*a*) $y = \pm 0.5$. (*b*) $y = 0.5$. $V_i = 0.75$.

Figure 8(*a*, *b*) shows the spanwise energy density $e_2(\beta)$ at $y = \pm 0.5$, obtained from the data in figures 4 and 5. The energy is concentrated in a range of wavenumbers between $\beta = 3$ and 4 at all downstream positions, with a drift towards slightly higher β at far downstream positions. This corresponds to a spanwise peak-to-peak distance slightly less than $2h$. At $x = 35$ and 50, a minor amount of energy is also found at $\beta = 7$, i.e. the first harmonic of the dominating spanwise wavenumber. It appears only in the lower part of the channel, where the perturbation amplitude is largest.

The downstream evolution of the energy distribution was obtained by undertaking z-traverses at $y = \pm 0.5$ at 15 different x-positions between 5 and 90. Figure 9 shows the evolution of the energy (E) per unit length normal to the wall in the plane

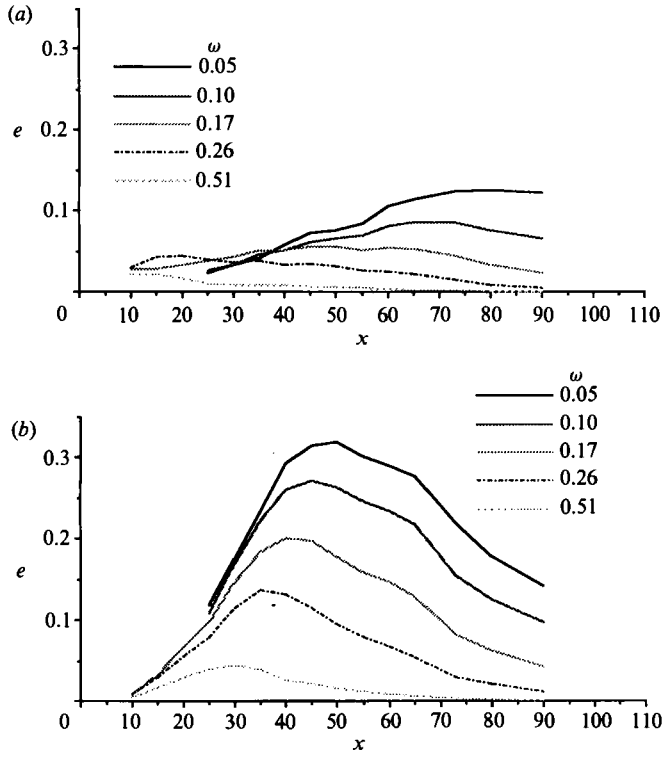

FIGURE 11. Evolution of $e_1(\omega)$ for specific frequencies between 0.05 and 0.5. $V_i = 0.75$. (*a*) $y = 0.5$. (*b*) $y = -0.5$.

$y = \pm 0.5$. In the upper part of the channel, the energy remains at an almost constant low level during the whole evolution, indicating that the decrease in local u-amplitude seen in figure 4 is balanced by the increase in streamwise extent. In the lower part of the channel, however, the energy increases linearly down to $x = 40$ and thereafter slowly decreases. Owing to the continuous elongation of the structure, the maximum in E occurs further downstream (at $x = 40$) than the maximum amplitude of u ($x = 30$). It is only far downstream that the energies in the upper and lower parts of the channel level out.

The energy distribution over frequencies, $e_1(\omega)$, is shown in figure 10(*a*, *b*) for $y = \pm 0.5$. In the initial phase, much of the energy at $y = \pm 0.5$ is due to the initial disturbance, which is reflected as a maximum in e_1 near e_1 near $\omega = 0.2$ for $x = 35$ in figure 10(*a*). As the disturbance moves downstream, more and more energy is concentrated at low values of ω, reflecting the elongation of the structure. This process is evident in both the lower and the upper parts of the channel. Figure 11 shows the energy evolution for specific frequencies between 0.05 and 0.5. The growth-decay behaviour is most evident in the lower half of the channel, where the energy densities have maxima between $x = 30$ (for $\omega = 0.5$) and $x = 50$ (for $\omega = 0.05$). In the upper part, only the frequencies below 0.2 experience growth, and the maxima occur further downstream than in the lower part. This non-uniformity between the upper and lower parts of the channel indicates that low-frequency energy is redistributed from the lower to the upper part of the channel during the downstream evolution.

In summary, more and more energy is concentrated at low frequencies during the downstream evolution of the perturbation structure. This trend corresponds to the

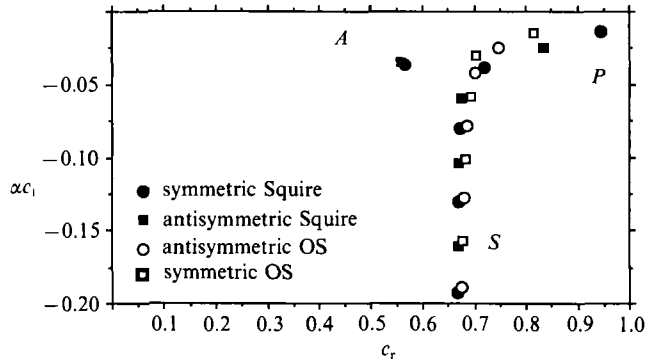

FIGURE 12. Spectrum of the temporal eigenvalues (c_r, αc_i) at $Re = 1600$, $\alpha = 0.1$, $\beta = 3.5$.

algebraic growth of zero wavenumber disturbances in the inviscid theory of Landahl (1980). It will be seen in the following that the longer lifetime of low-frequency components is also predicted by the viscous linear theory.

3.5. *Some aspects of the 3D Orr–Sommerfeld–Squire spectrum*

One of the main characteristics of the linear inviscid development of a 3D disturbance is that the propagation velocity of the perturbation structure is linked to the local velocity $U(y)$, and it was seen above (figures 6 and 7) that the perturbation structure studied in this experiment possesses this property. In the viscous theory, this feature is less evident, since the perturbation structure as a superposition of modes from the whole spectrum of the forced Squire equation.

Figure 12 shows the spectra of the Orr–Sommerfeld (OS) and Squire equations for plane Poiseuille flow at $Re = 1600$, $\alpha = 0.1$, $\beta = 3.5$, The eigenvalue problem was solved using a spectral collocation method (see Appendix for details of the calculations). The spectrum was classified by Mack (1976) into three branches named A, P and S. The most damped modes correspond to eigenvalues on the S-branch, which have real parts (c_r) approaching $\frac{2}{3}$. The corresponding mode shapes have their maxima about mid-way between the wall and the channel centreline. Eigenvalues on the P-branch modes have phase speeds between $\frac{2}{3}$ and 1, and are maximum near the centreline, whereas A-branch modes have low propagation velocities, and the mode shape is maximum near the walls. Classical stability theory is only concerned with the least stable OS mode (the TS wave), which is normally found on the A-branch. In contrast, the 3D initial growth of normal vorticity results because each 3D OS mode acts as a driving term in the 3D Squire equation, and excites the whole spectrum of Squire modes. The superposition of modes with different propagation velocities and cross-channel profiles will therefore result in a structure for which the propagation speed varies with y, the slowly moving parts near the wall representing contributions from the A-branch and the fast moving parts near the centreline contributions from the P-branch. Henningson (1991) found that OS modes on the P-branch give rise to a streaky structure, whereas A-modes ($c_r < \frac{2}{3}$) give a dispersive wave behaviour. An interesting feature of the spectrum shown in figure 12 is that there are no OS eigenvalues on the A-branch, i.e. there are no TS waves for the parameter combination of interest in the present experiment. Instead, the three least damped OS modes are located on the P-branch.

On the S-branch, the eigenvalues of the OS and Squire equations almost coincide, giving a near resonance in the coupling between the two equations. This is the reason

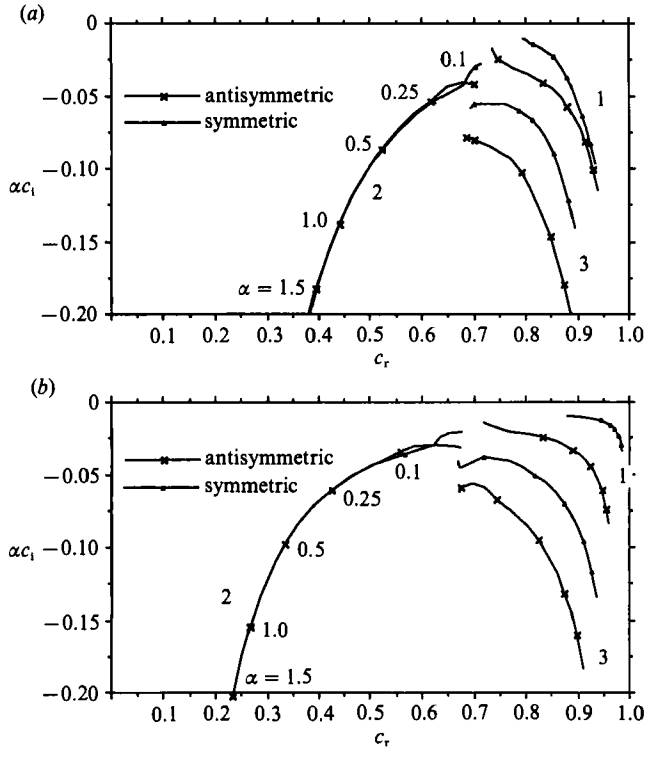

FIGURE 13. Variation of the eigenvalue spectra with α at $Re = 1600$, $\beta = 3.5$ for the three least stable modes. (*a*) Orr–Sommerfeld equation, (*b*) Squire equation.

why the S-branch modes are important in the 3D linear growth despite the fact that they are not the least damped ones. An OS mode with a symmetric mode shape will excite Squire modes having antisymmetric mode shapes. Note that the near-resonating OS and Squire modes on the S-branch have this symmetry relation.

Whereas the damping rate ($-\alpha c_i$) increases slowly with increasing β, it is highly sensitive to α. The decay rates of v and η are smallest for low α. This is shown in figure 13 for the three least stable modes of the spectra at fixed $Re = 1600$. For small α, the eigenvalues are located as in figure 12. With increasing α, the damping rates increase, and the eigenvalues are distributed further out on the A- and P-branches. This means that the low-wavenumber components of the initial disturbance have a longer lifetime and a more confined range of propagation velocities than the high-wavenumber components.

3.6. *The 3D linear initial growth*

The growth phenomenon is due to the fact that the whole spectrum of the Squire equation is excited. Since these modes are non-orthogonal, the energy of the sum of Squire modes is not the same as the sum of energies associated with the single modes. At $t = 0$, free and forced vorticity modes must combine so as to satisfy a given initial condition. The time evolution of this mode combination is the time evolution of the total normal vorticity. This is in brief the method of decomposition into eigenmodes suggested by Henningson (1991), which was used to obtain the results below (details of the calculations are given in the Appendix). Figure 14 shows that time evolution of the perturbation energy (T) associated with the normal vorticity for $\beta = 3.5$,

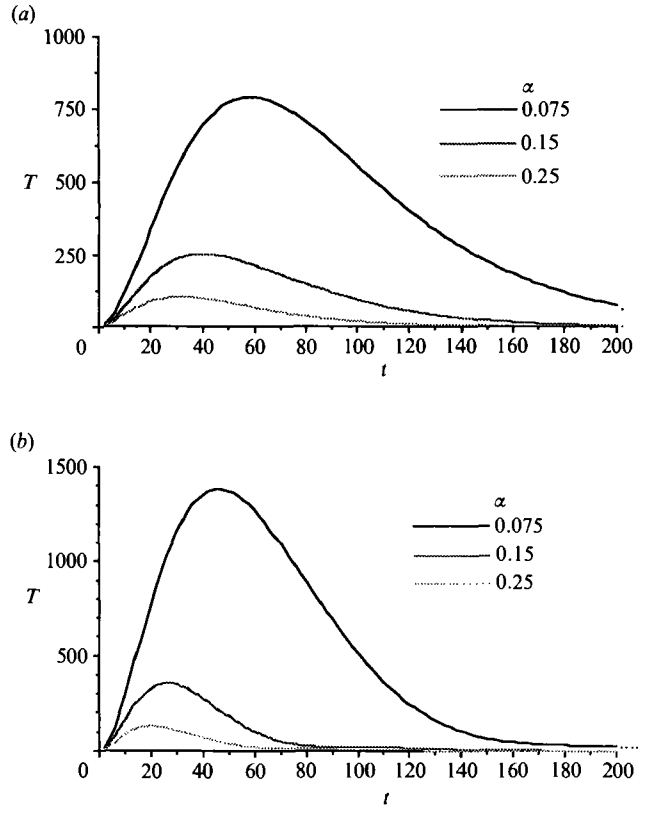

FIGURE 14. Time evolution of the normal vorticity energy at $Re = 1600$, $\beta = 3.5$, $\alpha = 0.075$, 0.15 and 0.25. (*a*) Least stable symmetric OS-mode driving, (*b*) antisymmetric mode driving.

$Re = 1600$, when only the least damped OS mode is used as a driving mode (this mode dominates the time evolution for small α). The perturbation energy grows up to a time (t_{max}), and thereafter decays. Figure 14 shows that t_{max} increases as α decreases, and that the growth time is larger when the driving mode is symmetric (figure 14*a*) than when it is antisymmetric.

Gustavsson (1991) showed that t_{max} is proportional to Re, and that it depends essentially on the parameter αRe. Klingmann & Alfredsson (1990) studied the downstream evolution of u at fixed y and z for various Re. They found that the amplitude of u showed the characteristic growth/decay behaviour, reaching a maximum at a time which is proportional to Re, in agreement with linear 3D viscous theory. In the present experiment, u was integrated in the spanwise direction and in time, so as to also take into account the growth caused by the continuous streamwise elongation. The result (figure 11) is qualitatively similar to that in figure 14. However, in order to make a quantitative comparison of t_{max} between experiment and theory, it would be necessary to assess the time evolution and wavenumber decomposition of the energy associated with the entire spatial structure of the perturbation, i.e.

$$\frac{1}{2}\int_0^\infty \int_{-1}^{1} \int_{-\infty}^{\infty} (u^2+v^2+w^2)\,\mathrm{d}x\,\mathrm{d}y\,\mathrm{d}z,$$

as a function of time. Since the present measurements are limited to two y-positions, $y = +0.5$, and the 'energy' E is an integral over time instead of over x, a comparison

between experimental and theoretical growth times can only be based on an estimate. We shall assume that v and w are much smaller than u, and that x and ω can be transformed to t and α by taking $\xi = \frac{2}{3}$ to be the typical propagation speed of the perturbation structure.

Figure 14 shows that for $\alpha = 0.075$ (corresponding to $\omega = 0.05$ in the experiment), the energy maximum occurs at $t_{\max} = 58$, and for $\alpha = 0.15$ ($\omega = 0.10$) at $t_{\max} = 40$. A disturbance propagating at $\xi = \frac{2}{3}$ will then be at $x_{\max} = 39$ and 27 respectively. This may be compared to the curves in figure 11, which show the time evolution of the low-wavenumber parts of the disturbance. The energy maximum of the low-frequency components ($\omega = 0.05$ and 0.10) are between $x_{\max} = 45$ (lower part of the channel) and $x_{\max} = 75$ (upper part). One could take into account that the onset of the algebraic growth is not at $x = 0$, but probably at about $x = 15$, giving an experimental $x_{\max}$ somewhere between 30 and 60. Hence the growth times obtained from the 3D linear initial-value problem are of a similar size to those observed in the experiment, but it is evident that the observed perturbation structure grows for a longer time than predicted by theory.

The results so far may be summarized as follows: the present experiments show that normal vorticity structures propagate at speeds between 0.55 and 0.85. The slower moving parts of the structure are found near the walls, whereas the front part is in the centre of the channel. This is consistent with the general features of the eigenvalue spectra of the OS and Squire equations. The region of strongest spanwise shear (normal vorticity) propagates at $\xi \approx 0.7$, and the cross-channel maximum of the disturbance is about midway between the wall and the centreline. These features are consistent with those of low α Squire modes, which for the parameters of this experiment are located mainly on the P- and S-branches. The largest growth rates and survival times of such modes are obtained when the streamwise wavenumber α approaches zero. Assuming that a point-like initial disturbance excites a flat spectrum of wavenumbers, the high-wavenumber part will decay quickly, whereas the low-wavenumber part will survive for a longer time and will be observable as growing elongated streaks. The streak structures observed in the experiments display this feature. They also show the growth/decay behaviour characteristic of the viscous linear mechanism. However, the low-frequency components grow for a longer time than predicted by linear theory. This may be the result of the nonlinear β-cascade described by Henningson *et al.* (1991), which leads to the regeneration of $\alpha = 0$ components, and hence an increase of the low-frequency contributions. The appearance of higher harmonics in β (figure 8*b*) at far downstream positions also supports this idea.

4. Near critical disturbances

In the previous section, a disturbance of subcritical initial amplitude was found to evolve into a V-shaped structure with 'legs' in the form of elongated streaks of normal and spanwise shear with a fixed spanwise spacing. The energy of the induced perturbation structure was seen to grow up to a streamwise position of about $x = 40$, and thereafter slowly decay. In the following section, results for an initial amplitude just below the level required to create a turbulent spot are presented. The development is followed through both the growth and decay stages.

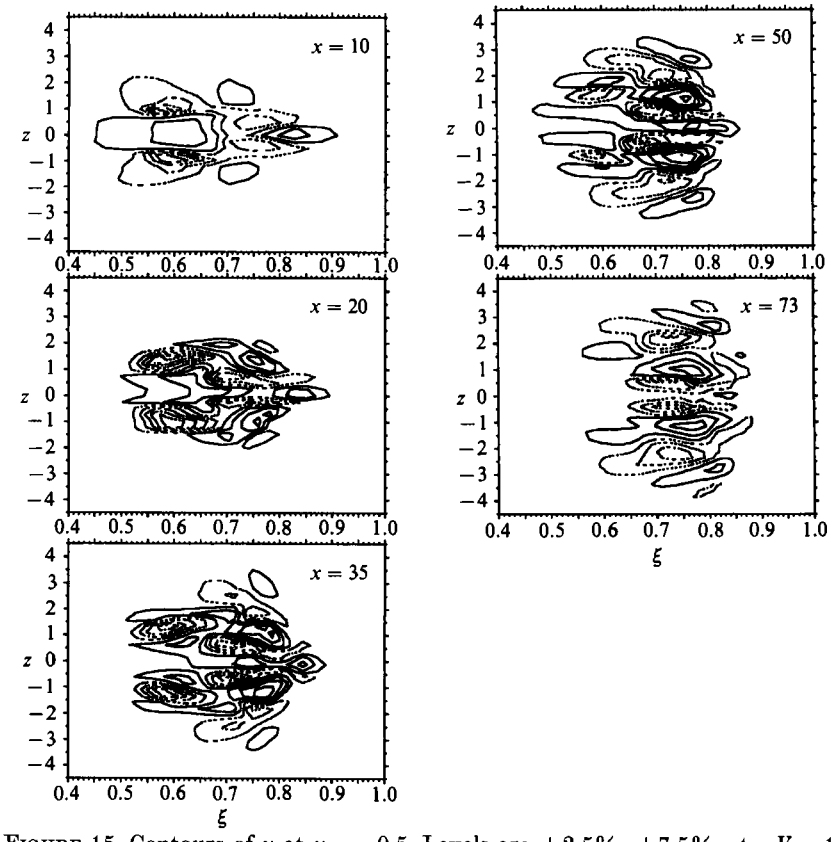

FIGURE 15. Contours of u at $y = -0.5$. Levels are $\pm 2.5\%$, $\pm 7.5\%$, etc. $V_1 = 1.4$.

4.1. *Evolution and spanwise structure*

Figure 15 shows the spanwise distribution of u measured at $x/h = 10$, 20, 35, 50 and 73 for the near critical disturbance. The normal position is midway between the channel centreline and the lower wall. The level spacing is 5% of U_{CL}. The virtual time origin t_0 was taken to be 2.2 (1.5 ms). Initially, the overall shape of a forward pointing V is similar to that in the subcritical case. However, a closer comparison at $x = 10$ (figure 15*a*), shows that the critical disturbance results in a more complex initial structure than in the subcritical case. Two interconnected low-velocity regions are seen at $z = \pm 0.5$ and ± 1.2, travelling at $\xi = 0.7$ and 0.6 respectively. These are stretched and separated downstream. The 'pinched off' low-speed legs at the rear are a feature introduced by the larger initial disturbance. In the subcritical case, streamwise gradients are only present at the front, and the front and rear parts do not grow apart until the decay phase (figure 5*e*). As in the subcritical case, the streaks do not spread in the spanwise direction, but the structure expands laterally by the appearance of new streaks on the flanks. These are skewed and part in the same way as the inner low-velocity streaks. The length and intensity of the streaks increase up to about $x = 50$, and thereafter begin to decay. Note that the streamwise extent of the structure is quite large in physical space. The 'aspect ratio' ($\Delta t U_{CL}/\Delta z$) of the streaks at $x/h = 50$ is about 20. The maximum local amplitude in u is above 20% at $x = 50$. Past $x = 50$, the rear streaks fade away, as does the whole central and rear region, leaving a structure with less streamwise variations at $x = 73$. However, the amplitude is still growing at the outer streaks, and new ones keep appearing. In the

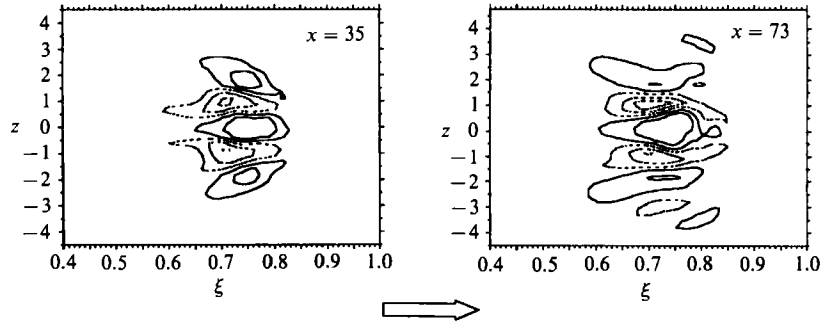

FIGURE 16. As figure 15 for $y = +0.5$.

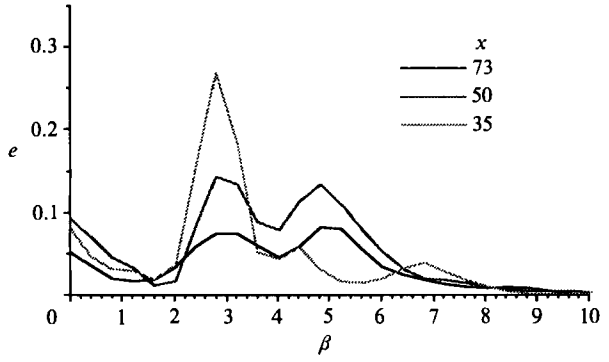

FIGURE 17. Spanwise energy distribution $e_2(\beta)$ at $y = -0.5$ obtained from data shown in figure 15.

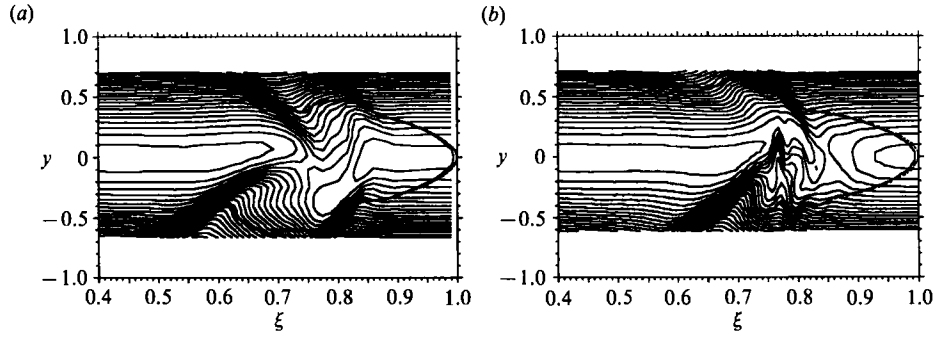

FIGURE 18. Cross-channel contours of $U = U_{\text{pois}} + u$ at $x = 35$. Levels are 0.025, 0.075, etc. $V_1 = 1.4$. (*a*) $x = 35$, $z = -1.2$. (*b*) $x = 50$, $z = -0.4$.

upper part of the channel (figure 16), the perturbation amplitude is lower and the streamwise extension is smaller. Streamwise gradients are almost absent, and the shape of the disturbance structure is similar to the one obtained in figure 4 with a lower input amplitude, although it is 2–3 times larger. There are no clear symmetry properties, but anti-symmetric structures seem to be dominating at $x = 73$ (see figures 15*e* and 16*b*).

Figure 17 shows the spanwise energy distribution at $x = 35$, 50 and 73. At all three x-positions, contributions from wavenumbers near 3 are seen, corresponding to the high and low velocity streaks at $z = \pm 1.2$. The energy at $\beta = 3$ decreases downstream, and contributions near $\beta = 5$ appear past $x = 50$. This corresponds to the fading of

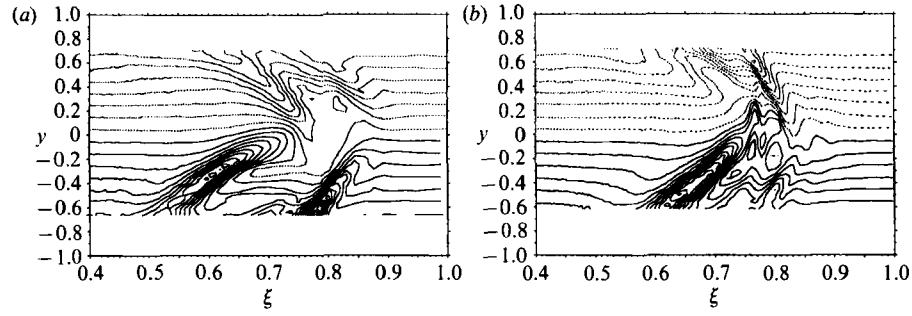

FIGURE 19. Cross-channel contours of $\partial U/\partial y$ at $x = 35$. Levels spacing is 0.2. $V_i = 1.4$. (*a*) $x = 35$, $z = -1.2$. (*b*) $x = 50$, $z = -0.4$.

the rear streaks at $z = \pm 1.2$ and the continued amplitude growth at the narrower streaks at $\xi = 0.65$–0.8 (see figure 15). By comparing the areas below the curves in figure 17, it is evident that the total energy E in the (t, z)-plane is largest at $x = 50$.

4.2. *Cross-channel distribution*

Figure 18 shows the cross-channel distribution of u along the lines $z = -1.2$ at $x = 35$ and $z = -0.4$ at $x = 50$. The former corresponds to the pinched-off low-velocity regions at the rear, and the latter to the central low-velocity streaks which can be seen in figure 15. As in the subcritical case, the shear layers are seen to connect at the local (distorted) mean velocity, i.e. $\xi = U(y)$. The corresponding isocontours of the total normal shear ($\partial U/\partial y$) are shown in figure 19. Figure 19(*a*) displays two inclined shear layers in the lower part of the channel with a low shear region in between, which corresponds to the intense high-speed regions at $z = \pm 1.2$. A weaker shear layer extends from the upper wall and interferes with the lower ones in the centre of the channel. Both layers are associated with negative streamwise gradient ($\partial u/\partial x < 0$). At $x = 50$, the low-velocity region at the rear is less intense, and the shear layer associated with it is less pronounced. Here, the central streaks are associated with the strongest shear, and the perturbations reach across the centreline. The shear layers in figure 19 resemble the high-shear layers preceding the formation of 'spikes' in the Klebanoff transition (cf. Nishioka, Asai & Iida 1981, or Krist & Zang 1987). The intensity and normal position of the shear layer are similar to those in the early stages in the simulation by Krist & Zang at $Re = 1500$ (see their figure 17). However, in the Klebanoff transition the high shear layer is associated with the 'head' of a $\wedge$-vortex, whereas the shear layer in figure 19(*a*) is located at the rear of the V-shaped structure and not at its head.

5. Critical disturbances and spot formation

Near the critical initial amplitude, a small increase can change the development of the perturbation structure from laminar decay to turbulence. When the initial disturbance amplitude was increased from $V_i = 1.4$ to 1.5, the velocity signals became less deterministic, and a wavelike instability appeared at the front of the structure. Upon further increase to $V_i = 1.6$, spikelike velocity signals were observed at the centreline of the channel. Both of these phenomena seem to be associated with the shear layers at the upstream legs of the V-shaped structure.

A spanwise view of the disturbance structure at $x = 50$, $y = -0.5$ for $V_i = 1.6$ is shown in figure 20. The motion is now less deterministic than in the previous cases.

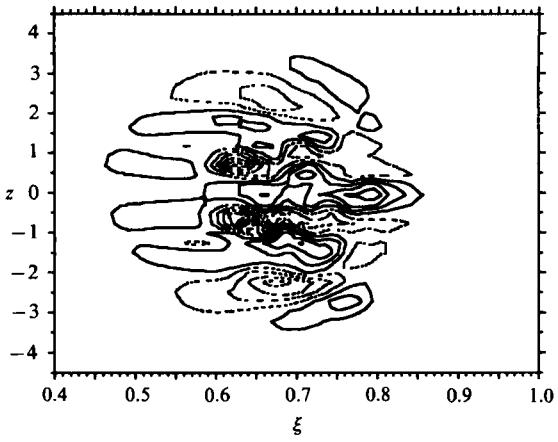

FIGURE 20. Contours of u at $y = -0.5$, $x = 50$ for critical initial disturbance ($V_i = 1.5$). Levels are $\pm 2.5\%$, $\pm 7.5\%$, etc.

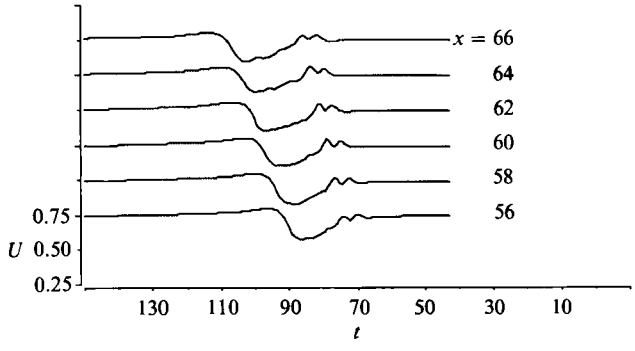

FIGURE 21. Traces of streamwise velocity (U) at $z = -0.5$, $y = -0.5$ for $V_i = 1.5$.

The overall structure is similar to the corresponding near-critical disturbance in figure 15(*d*). However, the rearward low-speed streaks at $z = \pm 1.2$ observed in figure 15(*d*) are not present any more, whereas the (negative) amplitude of u at the central low-speed streaks ($z = \pm 0.5$) is increased in comparison with figure 15(*d*). These streaks have distinct wavelike wiggles, indicative of an unsteady spanwise velocity component. Figure 20 also shows that the spanwise symmetry (which is still quite good in the near-critical case in figure 15*d*) is lost. Similar measurements at $x/h = 73$ show that the streaks are disrupted by non-deterministic motion, giving an apparent relaxation of the streamwise gradients in the ensemble average.

Ensemble average velocity traces collected at $z = -0.5$, $y = -0.5$ (figure 21) clearly show a wavy motion at the front of the flow structure. An initial disturbance amplitude of $V_i = 1.5$ was used so as to be able to follow the wave motion downstream without transition occurring. At this stage, the disturbance is no longer deterministic, and the amplitude of u at the low-speed streak as well as the amplitude of the waves differ greatly between realizations. In some cases, the low-speed streak is dissolved and only a large-amplitude wave motion is seen. The waves are stationary with respect to the front part of the low-speed regions, i.e. they propagate at the same speed ($\xi = 0.8$). Their angular frequency (ω), obtained after high-pass filtering of the velocity signal, is 1.3, i.e. an order of magnitude larger than for the low-speed streak itself.

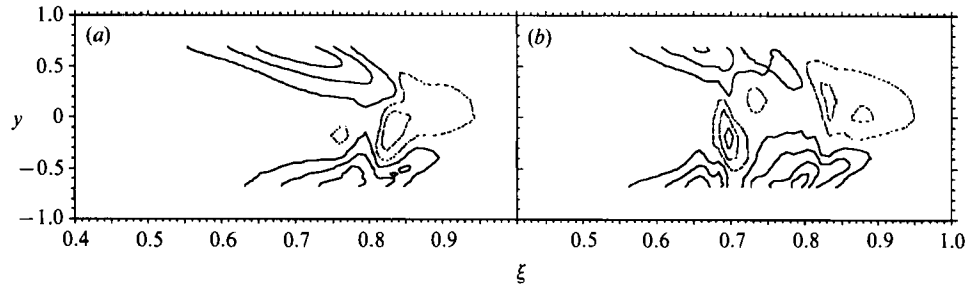

FIGURE 22. Cross-channel contours of u at $z = 0$, $x = 50$. Levels are $\pm 2.5\%$, $\pm 7.5\%$, etc. (a) Near critical disturbance, $V_1 = 1.4$. (b) critical disturbance, $V_1 = 1.6$.

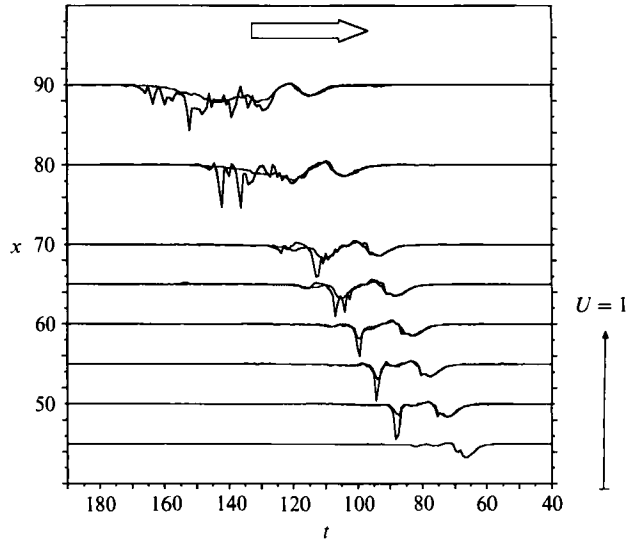

FIGURE 23. Traces of streamwise velocity (U) at $y = z = 0$ for $V_1 = 1.6$.

Figure 22 shows contour lines of ensemble-averaged streamwise perturbation velocity in a cross-channel view at $x/h = 50$, $z = 0$ for $V_1 = 1.4$ and 1.6. For $V_1 = 1.6$, the motion is no longer completely deterministic, so that the ensemble average gives a smeared-out picture of the actual velocity distribution in a single realization. The low-velocity region at the front near $y = 0$ represents the 'head' of the V-shaped structure. It is created by the initial disturbance and is present during the whole evolution of the disturbance structure. In figure 22(b), a more intense low-speed region is also seen at the rear (a corresponding region can only be vaguely seen in the near-critical case, see figure 22a). It appears as the passage of a spike in the velocity traces. Its location ($\xi = 0.70, y \approx -0.3$) corresponds to the position beneath the shear layer in figure 19(b), which was seen to be similar to the high-shear layers associated with spikes in the Klebanoff transition. However, the location of the spike and of the associated shear layer with respect to the entire flow structure is different.

Velocity traces at the centreline (figure 23) show the appearance of the spike and its downstream propagation. Dashed lines show ensemble averages, and full lines show selected individual realizations displaying enhanced non-deterministic features. At $x = 50$, a distinct spike appears at the rear of the structure. The time at which this

spike first appears is deterministic, whereas its amplitude varies, reaching in some cases about 25 % of U_{CL}. The propagation speed of the spike is estimated to be about 0.7. Further downstream, the spikes multiply and break down to small-scale turbulent motion. This cascade repeats itself, so that at $x/h = 90$ a fully turbulent rear part has formed. With increasing V_i, the process of spot formation takes place further upstream, e.g. for $V_i = 5.0$, a turbulent rear begins to form at $x = 20$. The further development of this turbulent spot has been described in detail in previous works (see Klingmann & Alfredsson 1990).

6. Concluding remarks

A point-like disturbance in the form of a localized short-duration jet introduced in plane channel flow at $Re = 1600$ was found to develop in three stages: (i) an initial phase, in which the jet lifts up slow moving fluid from the wall into the channel and sets up a flow with spanwise and normal shear, (ii) a phase of growth of the disturbance amplitude and streamwise extension and (iii) decay, alternatively, formation of a turbulent spot. The first of these stages is probably nonlinear. However, the large flow disturbance cause directly by the jet does not result in fluctuating turbulent motion. It is quickly damped and redistributed into downstream-pointing V-shaped structures associated with large spanwise and normal shear. This flow structure displays all the typical features of the linear 3D growth mechanism: (i) It elongates at a constant rate during its downstream travel; (ii) the shear layers propagate with the local streamwise velocity; (iii) there is no spanwise propagation, but there is a small spanwise spreading owing to the appearance of new streaks at the flanks of the perturbations structure; and finally (iii) the energy of the perturbation structure displays growth followed by decay on the timescale predicted by solving the viscous linear 3D initial-value problem. However, a feature which is difficult to explain within the framework of this theory is the well-defined spanwise wavenumber observed in the experiment. The asymptotic analysis of Gustavsson for $\alpha = 0$ gives the largest growth rates for β between 2 and 2.5, and one would expect to find these wavenumbers in an experiment which does not favour any specific spanwise wavenumber. However, in the present experiment (as well as in previous experiments using the same set-up reported by Klingmann & Alfredsson 1990) the energy is concentrated at β between 3 and 3.5 and at $\beta = 5$.

It is quite surprising that a large-amplitude initial disturbance can produce flow structure which seems to behave according to the linear 3D growth theory. The role of the initial jet is to set up a 3D structure with a spanwise variation. This can also be accomplished by other types of disturbances. For examples, in the numerical study by Henningson *et al.* (1991), two counter-rotating pairs of streamwise vortices with an amplitude small enough to guarantee linearity were used as an initial jet. This resulted in a flow structure quite similar to that seen in figure 5, without involving any nonlinear initial processes. The natural appearance of turbulent spots has been observed in channel flow even at Re below 1600 (cf. Carlson, Widnall & Peeters 1982), but little is known about the nature of the disturbances causing this transition. Uncontrolled background disturbances are not likely to have the concentrated form used in controlled experiments. It is possible, however, that large-scale 3D disturbances present under 'natural' flow conditions may initiate the linear 3D growth mechanism, resulting in flow structures similar to those studied in this work. An interesting issue to pursue would therefore be to assess what kind of initial disturbance is the most efficient in exciting the linear 3D growth.

At the present Re, an initial jet amplitude of the order of the maximum velocity in the channel is necessary to trigger a turbulent spot. This introduces an initial energy ($2h\pi R^2 V_i^2$, where R is the radius of the jet, and the jet velocity $V_i = 1.5$) of about 0.2 in non-dimensional units, which may be compared with the initial energy necessary to trigger TS wave transition. In numerical experiments on forced TS wave transition in plane channel flow, a wave amplitude of 0.1 is necessary to give transition at $Re = 1600$. The initial energy supplied ($\lambda^2 \int_{-1}^{1} v_{TS}\,dy$, where λ is the wavelength and v_{TS} the amplitude of the TS wave) is approximately the same as that supplied by the initial jet in the present experiments.

An initial jet which is just sufficient to trigger a turbulent spot gives a similar development up to a stage at which non-deterministic motion is observed in the form of spikes appearing at locations of high normal shear. The perturbation structure in this case differs from the subcritical one in that the upstream legs of the V-shaped structures are pinched off by negative streamwise gradients associated with intense inclined normal-shear layers. The presence of these shear layers could be tracked to the early stages of development. At the critical initial amplitude, spikes are observed at $z = 0$. Owing to the non-deterministic behaviour of the disturbance at this stage, it is difficult to give a precise picture of the cross-channel velocity distribution associated with the spike by traversing a single hot wire. However, ensemble-averaged data show that the first spike is associated with a low-speed region upstream of the head of the V-structure.

These results are closely related to the numerical results obtained by Henningson *et al.* (1991), and also bear a strong resemblance with those obtained by Amini & Lespinard (1982) under similar conditions in boundary-layer flow. The intense shear layers are similar to the high-shear layer associated with spikes in the Klebanoff transition. However, neither the shear layer nor the spike are related to the rest of the flow structure in the way that the Klebanoff high-shear layer and spike are related to the Λ-vortex. They propagate at $\xi = 0.7$, and it seems as if the spike constitutes the head of a newborn V-structure.

Another interesting observation at the transition stage is the appearance of a wavelike spanwise motion and the loss of spanwise symmetry. The waves are most clearly seen at the front of the structure. It is possible that these waves are related to waves observed at the stage of spot formation in boundary layers (cf. Gad-el-Hak, Blackwelder & Riley 1981; Chambers & Thomas 1983; Lismonde 1987). The 'incipient spot' investigated by Lismonde has many features in common with the present results. Also Chambers & Thomas observed that the wavy motion was associated with a lift-up of streaks from the wall, a description which is not inconsistent with the present observations.

This work is sponsored by the Fluid dynamic research program of the National Board for Industrial and Technical Development (NUTEK). Professor P. H. Alfredsson has contributed to the present work with invaluable advice, criticism and support. I also wish to thank Dr R. Shanthini, who has helped me to gain a deeper insight into 3D linear theory.

Appendix

The Orr–Sommerfeld (A 1) and the Squire (A 2) equations describe the stability of a *small* wave disturbance in the normal velocity (v) and vorticity (η) with streamwise and spanwise wavenumbers α and β, respectively ($k^2 = \alpha^2 + \beta^2$),

$$\frac{1}{\mathrm{i}\alpha Re}(\mathrm{D}^2-k^2)^2\hat{v}-[(U-c)(\mathrm{D}^2-k^2)-U'']\hat{v}=0, \tag{A 1}$$

$$\frac{1}{\mathrm{i}\alpha Re}(\mathrm{D}^2-k^2)\hat{\eta}-(U-\lambda)\hat{\eta}=\mathrm{i}\beta ReU'\hat{v}, \tag{A 2}$$

where 'hat' denotes the eigenfunction of the disturbance and c, λ are the complex eigenvalues of the OS-equation and Squire equation, respectively. U is a parallel shear flow with normal derivatives U' and U'', and D denotes $\partial/\partial y$. An arbitrary normal velocity disturbance can be written as a sum of the OS eigenmodes

$$v(x,y,z,t)=\sum_{n=1}^{\infty}\hat{v}_n(y)\exp[\mathrm{i}(\alpha x+\beta z)-\mathrm{i}\alpha c_n t],$$

whereas the normal vorticity is a combination of free and forced (by v) vorticity modes

$$\eta(x,y,z,t)=\sum_{m=1}^{\infty}\hat{\eta}_m(y)\exp[\mathrm{i}(\alpha x+\beta z)]\exp[-\mathrm{i}\alpha\lambda_m t]$$
$$+\sum_{n=1}^{\infty}\hat{\eta}_n^{\mathrm{part}}(y)\exp[\mathrm{i}\alpha x+\beta z)]\exp[-\mathrm{i}\alpha c_n t].$$

The phase velocities c_n and λ_m are eigenvalues (which will be taken as complex) and $\hat{v}_n(y)$ and $\hat{\eta}_m(y)$ are complex eigenfunctions of (A 1) and (A 2). $\hat{\eta}_n^{\mathrm{part}}$ are the eigenfunctions corresponding to the normal vorticity induced by $\hat{v}_n$.

The eigenvalue problems (A 1) and (A 2), subject to the boundary conditions

$$\hat{v}(\pm 1)=\mathrm{D}\hat{v}(\pm 1)=0, \quad \hat{\eta}(\pm 1)=0, \tag{A 3}$$

were solved by a spectral collocation method, in which v and η are expanded into a series of Chebyshev polynomials truncated at $M=50$ and evaluated at the normal positions

$$y_j=\cos\frac{\pi j}{2M-1} \quad (j=0,\ldots,M).$$

The boundary conditions (A 3) were applied at $j=0$ and 1, and symmetry conditions were imposed by selecting either symmetric or antisymmetric Chebyshev polynomials. The eigenvalue problem was solved using standard routines in double precision, and was found to agree to within all significant numbers with the test case given by Orszag (1971). For small enough α, the eigenvalues and mode shapes approach those analytically derived by Gustavsson (1991) for the asymptotic case $\alpha Re\to 0$ (for $Re=1600$, $\alpha<0.02$ is sufficiently small to consider αRe practically equal to zero).

Following Henningson (1991), the time evolution of normal vorticity for a specific wavenumber may be calculated as

$$\eta(x,y,z,t)=\sum_{n=1}^{\infty}\sum_{m=1}^{\infty}\hat{\eta}_m(y)D_{nm}\exp[\mathrm{i}(\alpha x+\beta z)](\exp[-\mathrm{i}\alpha c_n t]-\exp[-\mathrm{i}\alpha\lambda_m t]).$$

In the above expression, the initial normal vorticity present at $t=0$ is being taken as zero. The driving coefficients D_{nm} are obtained as

$$D_{nm}=\frac{K_n}{\alpha(c_n-\lambda_m)}\int_0^1\hat{\eta}_m\hat{v}_nU'\,\mathrm{d}y,$$

where K_n is a measure of the influence of the nth Orr–Sommerfeld mode in the initial distribution of v. The energy of η is defined as $T = \int \eta\eta^* \, dy$, where * denotes complex conjugate. In the data presented in §3, the normal vorticity was normalized by $\int \eta\eta \, dy$, and the normal velocity was normalized such that $v = 1$ at the position of its maximum. The time evolution of η was calculated using only the least damped OS-mode as the driving term and the 20 least stable Squire modes. K_1 was chosen arbitrarily as 0.01.

REFERENCES

Amini, J. & Lespinard, G. 1982 Experimental study of an 'incipient spot' in a transitional boundary layer. *Phys. Fluids.* **25**, 1743–1750.

Breuer, K. S. & Haritonidis, J. H. 1990 The evolution of a localized disturbance in a laminar boundary layer. Part 1. Weak disturbances. *J. Fluid Mech.* **220**, 569–594.

Breuer, K. S. & Landahl, M. T. 1990 The evolution of a localized disturbance in a laminar boundary layer. Part 2. Strong disturbances. *J. Fluid Mech.* **220**, 595–621.

Carlson, D. R., Widnall, S. E. & Peeters, M. F. 1982 A flow-visualization study of spots in plane Poiseuille flow. *J. Fluid Mech.* **121**, 487–505.

Chambers, F. W. & Thomas, S. W. 1983 Turbulent spots, wave packets, and growth. *Phys. Fluids.* **26**, 1160–1162.

Cohen, J. Breuer, K. S. & Haritonidis, J. H. 1991 On the evolution of a wave packet in a laminar boundary layer. *J. Fluid Mech.* **225**, 575–606.

Craik, A. D. D. 1971 Non-linear resonant instability in boundary layers. *J. Fluid Mech.* **50**, 393–413.

Criminale, W. O. & Kovasznay, L. S. G. 1962 The growth of localized disturbances in a laminar boundary layer. *J. Fluid Mech.* **14**, 59–80.

Gad-el-Hak, M., Blackwelder, R. F. & Riley, J. J. 1981 On the growth of turbulent regions in laminar boundary layers. *J. Fluid Mech.* **110**, 73–95.

Gaster, M. 1975 A theoretical model of a wave packet in the boundary layer on a flat plate. *Proc. R. Soc. Lond.* A **347**, 271–289.

Gaster, M. & Grant, I. 1975 An experimental investigation of the formation and development of a wave packet in a laminar boundary layer. *Proc. R. Soc. Lond.* A **347**, 253–269.

Grek, H. R., Kozlov, V. V. & Ramazanov, M. P. 1985 Three types of disturbances from the point source in the boundary layer. In *Laminar–Turbulent Transition* **2**, 267–272.

Gustavsson, L. H. 1991 Energy growth of three-dimensional disturbances in plane Poiseuille flow. *J. Fluid Mech.* **224**, 241–260.

Henningson, D. S. 1988 The inviscid initial value problem for a piecewise linear mean flow. *Stud. Appl. Maths* **78**, 31–56.

Henningson, D. S. 1991 An eigenfunction expansion of localized disturbances. In *Advances in Turbulence 3* (ed. A. V. Johansson & P. H. Alfredsson), pp. 162–169. Springer.

Henningson, D. S., Lundbladh, & Johansson, A. V. 1991 Bypass transition from localized disturbances. Submitted for publication

Henningson, D. S. & Schmid, P. J. 1991 A vector eigenfunction solution to the initial value problem in plane Poiseuille flow. Submitted to *Stud. Appl. Maths.*

Johansson, A. V. & Alfredsson, P. H. 1982 On the structure of turbulent channel flow. *J. Fluid Mech.* **122**, 295–314.

Kachanov, Y. S. & Levchenko, V. Y. 1984 The resonant interaction of disturbances at laminar–turbulent transition in a boundary layer. *J. Fluid Mech.* **138**, 209–247.

Klebanoff, P. S., Tidstrom, K. D. & Sargent, L. M. 1962 The three-dimensional nature of boundary-layer instability. *J. Fluid Mech.* **12**, 1–34.

Klingmann, B. G. B. 1991 Experiments on the growth of point-like disturbances in plane Poiseuille flow. In *Boundary Layer Stability and Transition to Turbulence* (ed. D. C. Reda, H. L. Reed & R. Kobayashi) *ASME FED* **114**, 137–143.

Klingmann, B. G. B. & Alfredsson, P. H. 1990 Turbulent spots in plane Poiseuille flow–velocity measurements. *Phys. Fluids* A **2**, 2183–2195.

KLINGMANN, B. G. B. & ALFREDSSON, P. H. 1991 On the development of a point-like disturbance in plane Poiseuille flow into a turbulent spot. In *Advances in Turbulence 3* (ed. A. V. Johansson & P. H. Alfredsson), pp. 182–188. Springer.

KRIST, S. E. & ZANG, T. A. 1987 Numerical simulation of channel flow transition. *NASA TP* 2667.

LANDAHL, M. T. 1975 Wave breakdown and turbulence. *SIAM J. Appl. Maths* **28**, 735–756.

LANDAHL, M. T. 1980 A note on an algebraic instability of inviscid parallel shear flows. *J. Fluid Mech.* **98**, 243–251.

LISMONDE, B. 1987 Champ de vitesse au bord d'attaque et dans le spot laminaire d'un écoulement sur une plaque plane. PhD thesis, L'Université Scientifique, Tequnique et Médicale de Grenoble.

MACK, L. M. 1976 A numerical study of the temporal eigenvalue spectrum of the Blasius boundary layer. *J. Fluid Mech.* **73**, 497–520.

NISHIOKA, M., ASAI, M. & IIDA, S. 1981 Wall phenomena in final stages of transition. In *Transition and Turbulence* (ed. R. E. Mayer), pp. 113–126. Academic.

ORSZAG, S. O. 1971 Accurate solution of the Orr–Sommerfeld stability equation. *J. Fluid Mech.* , 689–703.

TSO, J., CHANG, S. I. & BLACKWELDER, R. F. 1990 On the breakdown of a wave packet disturbance in a laminar boundary layer. In *Laminar–Turbulent Transition* (ed. D. Arnal & R. Michel), pp. 199–214. Springer.

VASUDEVA, B. R. 1967 Boundary layer instability experiment with localized disturbance. *J. Fluid Mech.* **29**, 745–763.

WYGNANSKI, I. 1981 The effect of Reynolds number and pressure gradient on the transitional spot in a laminar boundary layer (ed. J. Jimenez) *Lecture Notes in Physics*, vol. 136, pp. 305–332. Springer.

ZELMAN, M. B. & SMORODSKY, B. V. 1990 On the wave packets interaction in a transitional boundary layer. In *Laminar–Turbulent Transition 3* (ed. D. Arnal & R. Michel), pp. 285–290. Springer.